Monthly Notices of the ROYAL ASTRONOMICAL SOCIETY

MNRAS **516,** 540–549 (2022) https://doi.org/10.1093/mnras/stac2143
Advance Access publication 2022 August 1

Searching for stellar flares from low-mass stars using ASKAP and *TESS*

Jeremy Rigney [1,2,3★] Gavin Ramsay [2] Eoin P. Carley,[1] J. Gerry Doyle,[2] Peter T. Gallagher [1] Yuanming Wang [4,5,6] Joshua Pritchard [4,5,6] Tara Murphy [4,6] Emil Lenc [5] and David L. Kaplan [7]

[1]*Astronomy & Astrophysics Section, DIAS Dunsink Observatory, Dublin Institute for Advanced Studies, Dublin, D15 XR2R, Ireland*
[2]*Armagh Observatory and Planetarium, College Hill, Armagh BT61 9DG, UK*
[3]*School of Mathematics and Physics, Queen's University Belfast, University Road, Belfast BT7 1NN, UK*
[4]*Sydney Institute for Astronomy, School of Physics, University of Sydney, NSW 2006, Australia*
[5]*Australia Telescope National Facility, CSIRO, Space and Astronomy, PO Box 76, Epping, NSW 1710, Australia*
[6]*ARC Centre of Excellence for Gravitational Wave Discovery (OzGrav), PO Box 218, Hawthorn, VIC 3122, Australia*
[7]*Department of Physics, University of Wisconsin-Milwaukee, P.O. Box 413, Milwaukee, WI 53201, USA*

Accepted 2022 July 27. Received 2022 July 27; in original form 2022 April 13

ABSTRACT

Solar radio emission at low frequencies (<1 GHz) can provide valuable information on processes driving flares and coronal mass ejections (CMEs). Radio emission has been detected from active M dwarf stars, suggestive of much higher levels of activity than previously thought. Observations of active M dwarfs at low frequencies can provide information on the emission mechanism for high energy flares and possible stellar CMEs. Here, we conducted two observations with the Australian Square Kilometre Array Pathfinder Telescope totalling 26 h and scheduled to overlap with the *Transiting Exoplanet Survey Satellite* Sector 36 field, utilizing the wide fields of view of both telescopes to search for multiple M dwarfs. We detected variable radio emission in Stokes *I* centred at 888 MHz from four known active M dwarfs. Two of these sources were also detected with Stokes *V* circular polarization. When examining the detected radio emission characteristics, we were not able to distinguish between the models for either electron cyclotron maser or gyrosynchrotron emission. These detections add to the growing number of M dwarfs observed with variable low-frequency emission.

Key words: stars: activity – stars: flare – stars: low-mass – radio continuum: stars.

1 INTRODUCTION

M dwarfs are core hydrogen-burning stars with masses between 0.07 and 0.6 M$\odot$ and surface temperatures ranging from 2500 K (M9.5) to 3700 K (M0) (Rajpurohit et al. 2013). They are the most common type of star in the Milky Way, making up an estimated 70 per cent of the stellar population (Henry et al. 2006; Bochanski et al. 2010). High rotation rates (< 10 d) and convective cores, particularly in late-type M dwarfs (> M4), generate complex powerful global magnetic fields with large stable star spots (Günther et al. 2020; Kochukhov 2021). Hence, these stars can regularly produce flares with energies in excess of $\sim 10^{32}$ erg up to $\sim 10^{35}$ erg and superflares with energies surpassing 10^{36} erg (Osten et al. 2010; Davenport 2016; Schmidt et al. 2019; Ramsay et al. 2021). It is thought these stellar flares occur via the same magnetic reconnection process as observed in solar flares, and this process also leads to the expulsion of plasma into the stellar atmosphere, known as a stellar coronal mass ejection (CME). While CMEs are a regular occurrence on the Sun, there are relatively few observational confirmations of stellar CMEs. A potential means of observing stellar flares and CMEs is through radio observations. Although there have been observations of stars that are consistent with being caused by CMEs, there has been no unambiguous detection of a Type II like burst or CME signature on a star other than the Sun (e.g. Mullan & Paudel 2019; Zic et al. 2020). Routine detections of such radio bursts would open up new avenues of flare and CME research on M-dwarf stars, and new-fields of exo-space weather.

On the Sun, flares and CMEs are associated with the acceleration of energetic electrons, producing emission from gamma-ray to radio. The mildly relativistic electrons can often be associated with bursts of radio emission. For example, Type III bursts are produced from mildly relativistic electrons escaping on open magnetic fields (Reid & Ratcliffe 2014), Type IVs are associated with energetic electrons trapped in either the flare or CME (Carley et al. 2021), while Type II bursts are generated from CME-driven shocks (Nelson & Melrose 1985; Maguire et al. 2020; Morosan et al. 2021). Given the fact these radio bursts can be coherent emission, they have flux densities averaging 10^8 Jy and can be as high as 10^{11} Jy (Cerruti et al. 2008; Raja et al. 2022). Radio bursts can be used as a diagnostic of plasma density, plasma turbulence, electron energies and the sites of particle acceleration during the eruptive process. In other cases, the radio bursts can be associated with gyrosynchrotron emission (particularly the Type IVs; Carley et al. 2017) and in rarer cases the flares and CMEs have also been known to be associated with electron cyclotron maser (ECM) emission (Liu et al. 2018; Carley et al. 2019; Morosan et al. 2019).

The close association of solar radio bursts with the flare-CME energy release process, and the high intensity of the coherent radio

★ E-mail: jeremy.rigney@dias.ie

emission, has prompted many searches for analogous activity on Sun-like and M-dwarf stars. Searches for such radio activity have tended to concentrate efforts at higher frequencies, e.g. 1 GHz with telescopes such as the VLA or Arecibo (Stepanov et al. 2001; Osten & Bastian 2006; Villadsen & Hallinan 2019), with some success in detecting bursts with flux densities of 10–100 mJy. Only a handful of studies have been able to detect such bursts at lower frequencies, e.g. the detection of 60 mJy radio bursts at 154 MHz from UV Ceti using MWA (Lynch et al. 2017), or 21 mJy radio bursts showing drifting features using VLA P-band (230–470 MHz) observations (Crosley & Osten 2018). Further, Callingham et al. (2021b) observed M dwarfs with peak radio fluxes reaching 205 mJy at 170 MHz. Recently, data from telescopes such as the LOw Frequency ARray (LOFAR; e.g. Callingham et al. 2021a) and the Australian Square Kilometre Array Pathfinder Telescope (ASKAP; e.g. Zic et al. 2020) have been used to search for stellar-analogues to Type II and IV emission from M dwarfs.

In terms of the expected emission mechanism of stellar radio bursts, much of the current research observing M dwarfs at low frequencies has centred on ECM. This beamed coherent emission can be characterized by a high degree of circular polarization with a high ($> 10^{12}$ K) brightness temperature (Kellermann & Pauliny-Toth 1969; Melrose & Dulk 1982; Dulk 1985; Vedantham 2021). This is thought to emerge from flaring activity (Lynch et al. 2017; Zic et al. 2020) or auroral processes (Kuznetsov et al. 2012; Metodieva et al. 2017; Zic et al. 2019; Callingham et al. 2021b) and its characteristics help to better understand the radio emission sources and diagnostics such as magnetic fields of M dwarfs (Callingham et al. 2021a). Recent detections of circularly polarized long duration radio emission from a quiescent M dwarf may even be indicative of star–planet interactions, similar to the Jupiter-Io system (Vedantham et al. 2020; see Marques et al. 2017 for a detailed overview of Jupiter decametric emission). Recently, more comprehensive studies utilizing survey data have yielded statistics from an increasingly large number of M dwarfs, further helping to constrain and categorize the dominant emission mechanisms of these active stars. Villadsen & Hallinan (2019) detected 22 radio bursts from 5 active M Dwarfs using the VLA, concluding that all bursts were likely produced via a coherent emission process due to high (>50 per cent) circular polarization.

Callingham et al. (2021a) detected 19 M dwarfs in the LOFAR Two Meter Sky Survey, all with high degrees of circular polarization and high brightness temperatures indicative of either plasma emission or ECM. They highlight that gigahertz detections typically fall into two categories, either long-duration low polarization or polarized short-duration bursts. It is clear that M dwarfs can produce low-frequency radio emission through high energy events related to flares and active regions on the stellar surface.

Pritchard et al. (2021) conducted a search for circularly polarized stars within the Rapid ASKAP Continuum Survey (RACS; McConnell et al. 2020), detecting among their results 9 M dwarfs with emission centred at 887.5 MHz and a 288 MHz bandwidth. The majority of these sources had high (>50 per cent) circular polarization. Combined with high brightness temperature calculations, the authors concluded that coherent processes likely drive the emission from these sources.

Active M dwarf CMEs are expected to occur much more frequently when compared to the solar flare-CME scale (Crosley & Osten 2018; Moschou et al. 2019). Hence, the relatively low number of detections of stellar radio bursts is surprising (Crosley et al. 2016). It is speculated that the high magnetic field strength of M dwarfs are high enough to constrain plasma release (Alvarado-Gómez et al. 2018; Kochukhov 2021), or that the local Alfvén speeds are too fast for CME shocks to occur (Villadsen & Hallinan 2019). This would inhibit the production of shock-related radio emission, for example. Some stellar CME signatures may still be detectable at radio frequencies, albeit as a faint long duration gradual brightening rather than the more recognized emission of a solar type II radio burst (Alvarado-Gómez et al. 2019). Further exploration of this theory suggests the radio emission may be pushed beyond detectable limits with current ground-based radio telescopes. The magnetic suppression could push the shock into the lower density outer corona and the resulting Type II-analogous emission is <20 MHz and below 1 mJy (below the ionospheric cut-off and sensitivity limits of current radio telescopes) and likely not-detectable (Alvarado-Gómez et al. 2020). Recent simulations hint at detectable radio emission from high energy stellar CMEs at very low frequencies (Fionnagáin et al. 2022), yet sustaining regular plasma ejections yields high mass-loss rates (Osten & Wolk 2015). This conflicts with the long projected lifetimes of low-mass stars.

Multiwavelength observations of M dwarf activity have helped paint a clearer picture of flare energies, emission mechanisms, magnetic field strengths (Murphy et al. 2013), star-spot coverage, stellar activity-rotation period relation as well as many other factors that can help in understanding space weather in possible exoplanetary systems.

With more detections of M dwarfs in the low-frequency radio regime, a number of possible emission mechanisms have been suggested. Pope et al. (2021) examined *Transiting Exoplanet Survey Satellite* (*TESS*) light curves of the 19 M dwarfs detected with LOFAR (Callingham et al. 2021a) and found that for M dwarfs showing no flare activity but significant radio emission, magnetic processes were more likely to be driving the radio emission rather than coronal processes. Two targets were contemporaneously observed with LOFAR and *TESS* for 8 h, although no flares were detected in either the optical or radio bands during this time.

However, the relation between radio emission and activity on these stars requires more investigation, particularly examining the connection between energy release across the electromagnetic spectrum. The aim of this work was to utilize simultaneous ASKAP and *TESS* observations of two regions in the Southern Hemisphere in the search for variable emission from multiple active M dwarfs. Observing at both radio and optical wavelengths allowed for any detected radio emission to be correlated with optical flaring activity or period of quiescence on the stars. We made use of *TESS* Sector 36 observations that contain pointings at latitudes suitable for simultaneous observations with the ASKAP radio telescope. This work builds on previous observations of M dwarf observations at <1 GHz, such as Pritchard et al. (2021), Zic et al. (2019, 2020), and Villadsen & Hallinan (2019).

In Section 2, the observations and data reduction is described for both data sets. In Section 3, we report on the results of the observations and detection of M dwarfs. Section 4 covers the discussion on our findings. Section 5 contains the summary and conclusions of the paper.

2 OBSERVATIONS AND DATA REDUCTION

2.1 Australian Square Kilometre Array Pathfinder Telescope

The ASKAP (Johnston et al. 2008; Hotan et al. 2021) telescope is a 36 dish radio interferometric array constructed in a radio quiet zone in Western Australia. The system observes from 700–1800 MHz. The array has a 6 km maximum baseline, and has a 30 square degree

field of view. ASKAP is primarily designated as a survey telescope, with a current survey mapping radio sources in the southern sky to a sensitivity of < 0.25 mJy (McConnell et al. 2020). For the current study, Directors Discretionary Time was used to take advantage of the overlapping observing region with *TESS* (see Section 2.2).

Observations were scheduled for the dates 20-03-2021 (ID SB25035) and 21-03-2021 (ID SB 25077). The frequency range was centred at 888 MHz with a bandwidth of 288 MHz, in 1 MHz channels (see Table 1). Each observation totalled 13 h at 10-s time resolution with the data being initially processed using the current ASKAPsoft pipeline (see Cornwell, Voronkov & Humphreys 2012; Murphy et al. 2021 for details). Further processing to produce images and dynamic spectra was completed using the *Common Astronomy Software Applications* (CASA package; McMullin et al. 2007). Full 13-h time-range integrations were used to produce Stokes *I* and *V* images with a resulting mean $\mathrm{RMS}_I = 0.024$ mJy beam^{-1} and $\mathrm{RMS}_V = 0.021$ mJy beam^{-1}. The resulting 13 h Stokes *I* images were then searched for sources using the *SELAVY* (Whiting & Humphreys 2012) routine.

The coordinates of significant ($>4\sigma$) sources were compared to the active M dwarf catalogue of Günther et al. (2020): four sources were identified from this processing (see Fig. 3). The calibrated beam visibilities containing the detected sources were then selected for further processing. Following the method of section 2.2.1 in Wang et al. (2021) a multifrequency and multiscale synthesis model image was created for each beam using the CASA `tclean` function. The model images were converted to model visibilities, then subtracted from the original calibrated visibilities. We imaged these model-subtracted visibilities across the full frequency range in 10 min integrations that identified variable sources in the field and subtracted non-varying sources. The same process was repeated for Stokes *V*, *Q*, and *U*. The polarization leakage values were estimated to be approximately the same as that found in Zic et al. (2019) (i.e. *I* to *V*: ~ 0.1 per cent, *I* to *Q*: 0.5 per cent, *I* to *U*: 1.5 per cent). With sources in the centre of the field, the effect of polarization leakage is less than the effect from RMS noise. None of the sources detected were near the edge of either SB25035 or SB25077, thus the leakage is taken to be negligible when compared to the contribution of noise.

The peak calibrated flux density was obtained from the central pixel of the 2D Gaussian at the source coordinates. This, with the addition of the model subtracted flux density, was used as the total flux density for an unresolved point source for each 10 min image. The RMS for each image was also calculated and averaged across all images to determine the noise threshold for a detection. The results of this analysis are presented in Section 2 (see Fig. 4).

Dynamic spectra were created from visibility data using CASA. The visibilities at each target coordinate were masked and a model of the field was created. This was then subtracted from the raw field visibilities, leaving only the target of interest visibilities. Phase centre rotation, baseline averaging and time and frequency averaging were performed to generate the final dynamic spectra for the targets. The data were averaged down to 20 MHz frequency bands and 10 min integrations. A circularly polarized radio burst was detected in the Stokes *V* dynamic spectrum for one of the stars.

2.2 Transiting Exoplanet Survey Satellite

The *TESS* (Ricker et al. 2015) was launched in 2018 April with a primary mission of searching for exoplanets via the transit method around low-mass stars. In its first 2 yr, *TESS* completed a near all-sky survey observing more than 200 000 stars with a cadence of 2 min. In Year 3 a sample of stars were also observed with a cadence of 20 s. *TESS* observes in Sectors corresponding to observing one field for 26 d during two Earth orbits. Observations of Sector 36 took place between 2021 March 7th and April 1st. The ASKAP observations were scheduled to align with Sector 36.

We downloaded the calibrated light curves for each of our four target stars from the MAST data archive.[1] We examined the light curve derived using the simple aperture photometry (`SAP_FLUX`) and the light curve that has been detrended and corrected for instrumental effects (`PDCSAP_FLUX`). Detrended points that did not have `QUALITY = 0` were removed and each light curve was normalized by dividing the flux of each point by the mean flux of the star.

We show the *TESS* light curve of each source in Fig. 1 indicating the times where ASKAP data were obtained. Each light curve shows a clear modulation in flux over time that is very likely a signature of the stellar rotation period caused by star-spots rotating into and out of view. For source WOH S 2 (TIC 29779873) and HD 270712, the observations at the start of the run were of relatively poor quality. We determined the period of the modulation using the Lomb Scargle periodogram and the Analysis of Variance deriving (consistent) periods of 0.8544 d (CD-56 1032A); 0.3244 d (TIC 55497266) and 2.62 d and 0.200 d in WOH S 2 (TIC 29779873). *Gaia* shows there are two sources near WOH S 2 ($G = 14.2$ and $G = 14.9$) that are 1.28 arcsec apart and therefore fall into the same *TESS* pixel (21 arcsec per pixel). One source has a *Gaia* ($BP - RP$) colour consistent with an M dwarf but the other star has no colour information. The *TESS* light curve of WOH S 2 is therefore a combination of both stars. The rotation rate calculated from the *TESS* data for HD 270712 was 0.5264 d; however, this cannot be attributed to either M dwarf in the visual binary.

There were no clear signatures of flares in the *TESS* light curves within the time-range of the ASKAP observations. However, there is one raised 'notch' like feature seen in CD-56 1032A (Fig. 1, although it does not have a profile typical of flares). Comparing the light curve at the same rotational phase during the rest of the *TESS* observations (Fig. 5), we note that flare events have been observed at this rotational phase (and others) during earlier and later rotations. We speculate that this notch like feature may be related to active regions that are visible at this rotation phase, although it is unclear why other flare active regions do not show this feature.

Although there are no clear flares in the time interval where simultaneous ASKAP data were obtained we searched all the available *TESS* data for flares. To search for flares in the light curves, we removed the signature of the rotational modulation using a routine in the LIGHTKURVE package (Lightkurve Collaboration 2018). We then searched these flattened light curves for flares using the ALTAIPONY[2] suite of software, which is an update of the APPALOOSA (Davenport 2016) software package. We obtained the stars bolometric luminosity from the TIC V8.0 catalogue (Stassun et al. 2019) that uses *Gaia* DR2 (Gaia Collaboration 2018) and other information to determine the luminosities. (For WOH S 2 that does not have a luminosity in TIC V8, we used the *Gaia* ($BP - RP$) colour to estimate its luminosity by comparison with other M dwarfs of a similar colour). To determine the luminosity of the flares, we take the equivalent duration of the flare, calculated using ALTAIPONY, and multiply this by the stellar quiescent luminosity. We assume that the temperature of the flare is $\sim$12 000 K and that the fraction of the emitted flux which falls within

[1] https://archive.stsci.edu/tess/
[2] https://altaipony.readthedocs.io/en/latest

Table 1. The observation log of the ASKAP data that were used in this study.

Obs. ID	Obs. start (UT)	Obs. end (UT)	Duration (h)	Freq. range (MHz)	Freq. res. (MHz)	Time res. (s)
SB25035	2021-03-20 03:10:58	2021-03-20 16:00:31	12.826	700–1000	1	10
SB25077	2021-03-21 03:36:49	2021-03-21 16:26:22	12.826	700–1000	1	10

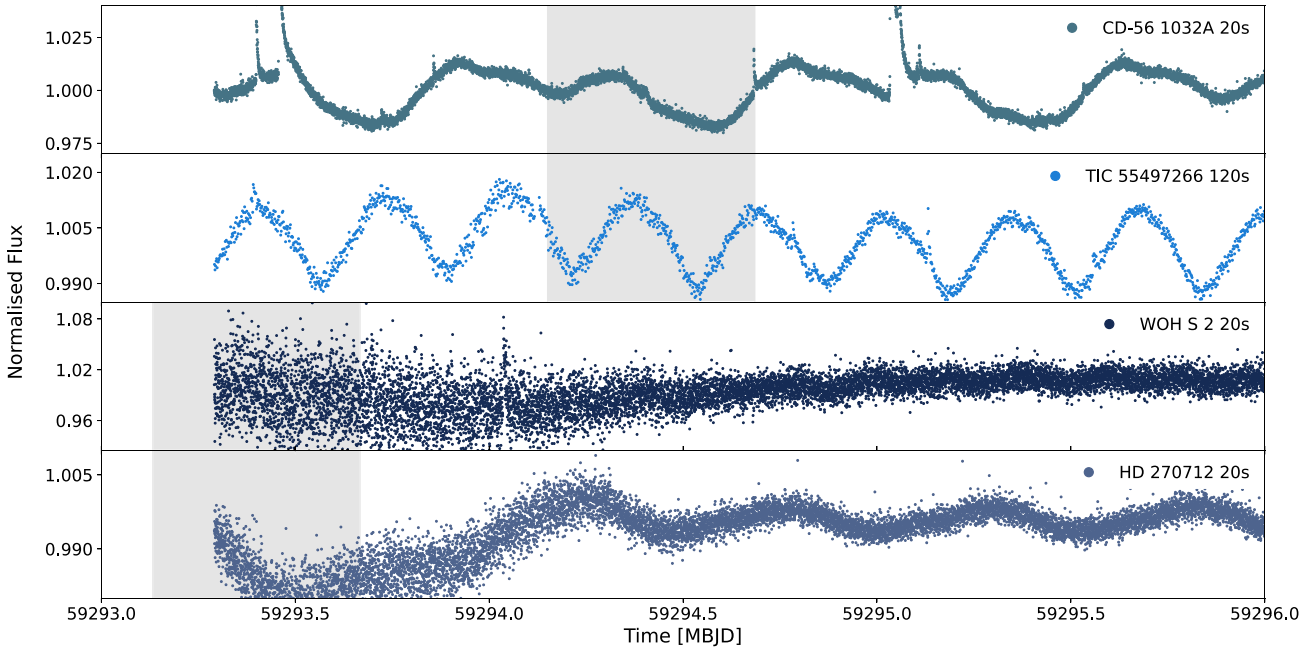

Figure 1. *TESS* Simple Aperture Photometry (SAP) optical light curves for the four detected M dwarfs. This figure illustrates the different characteristics of the light curves of each star, with clear periodic dips consistent with the presence of large star spots. The shaded region indicates when the stars were observed simultaneously with ASKAP and *TESS*. Note the missing WOH S 2 and HD 270712 data were due to a scheduled *TESS* data down-link between orbits 79 and 80 of Sector 36 observations. CD-56 1032A and TIC 55497266 were observed during ASKAP observing I.D. SB25077. WOH S 2 and HD 270712 were observed during I.D. SB25035. Only 120 s cadence *TESS* data were available for TIC 55497266. The region of HD 270712 co-observed with ASKAP has a very poor light curve severely impacted by instrumental effects, and was not used in this research. The light curve of WOH S 2 was similarly affected.

the *TESS* pass-band is ∼0.14 (Schmitt et al. 2019), thus requiring a multiplication of 7.1 to obtain the bolometric energy.

Using Cycle 1 and 3 *TESS* data, we determined the flare rate and energies and obtained the flare frequency distribution for three of the stars in each year of observation and this is shown in Fig. 2. There is good general agreement between the flare rate for the stars observed one year apart, with flares of energy 10^{34} erg observed approximately every day in CD-56 1032A (unfortunately not during our ASKAP observations) and every tens of days of WOH S 2, with TIC 55497266 showing small flares every few days. There is a small decline in the number of flares seen in CD-56 1032A during Cycle 3 compared to Cycle 1. Since the stars have a range in brightness and distance, they are not equally sensitive to flares $<10^{34}$ erg. However, the rate of flares with energies $>10^{34}$ erg place CD-56 1032A and TIC 55497266 in the region where high energy flares may deplete the Ozone layer of any Earth-like planet in the host stars habitable zone (see e.g. Günther et al. 2020; Ramsay et al. 2021).

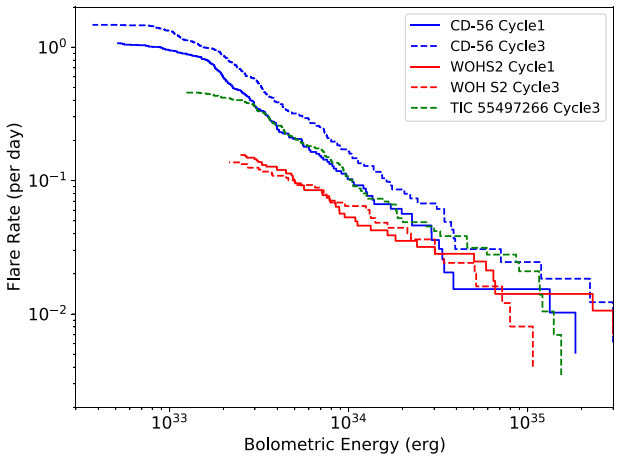

Figure 2. The flare frequency rate for the three stars in this study. It indicates how often a flare of a certain energy is observed. Two stars were observed in Cycles 1 and 3. These flare rates have been calculated from the first two months of *TESS* data.

3 RESULTS

Using the work of Pecaut (2013) we identified 46 possible M dwarf targets identified within the two regions observed[3]. The comparison between radio source coordinates and *Gaia* coordinates (proper motion corrected) revealed four targets detected by ASKAP with *TESS* light curves (Table 2) (Fig. 3).

Of these four sources detected in this study, two were detected in Stokes *I* images only: CD-56 1032A and TIC 55497266. One source was detected in both Stokes *I* and Stokes *V*: WOH S 2. One source was detected with faint quiescent Stokes *I* emission and a 100 per cent circularly polarized burst (HD 270712) (Table 3). There were no optical flares that coincided in time with radio events that were significantly above the mean Stokes *I* or *V* flux density. However, in CD-56 1032A, a radio peak coincided with a raised 'notch' like feature in the optical light curve: see Fig. 4 for the ASKAP and *TESS* light curves. No discernible radio burst features were observed in the generated dynamic spectra for three of the sources. A faint vertical radio burst was detected in the Stokes *V* dynamic spectrum of HD 270712. We now go on to discuss the details of the results for each of the four stars in turn.

Brightness temperatures were calculated using equation (1), from Dulk (1985) and also used in Zic et al. (2019):

$$T_b = S\left(\frac{c^2}{\nu^2}\right)\left(\frac{1}{2k}\right)\left(\frac{d^2}{A}\right)(1\times 10^{-26}), \quad (1)$$

where S is the peak flux density in Janskys, ν is the observed frequency (in this paper, the central frequency of 888 MHz is used), k is the Boltzmann constant, d is the distance in meters, and A is the area of the region where the emission is thought to originate. For the purposes of estimating the brightness temperature the full disc of each star is used as the emitting region.

3.1 CD-56 1032A (TIC 220433363)

Source CD-56 1032A was detected in the second observation field SB25077 data from the 2021 March 21st in Stokes *I* with 13 h of integrated images giving a mean flux density of 0.32 ± 0.01 mJy beam^{-1}. There was no associated Stokes *Q*, *U*, nor *V* emission detected from the source in this observation. The 10-min integrated light curve in Fig. 4(a) shows a peak radio flux density of 2.89 ± 0.23 mJy beam^{-1}. We calculated a brightness temperature of $2.4 \times 10^{10} \pm 0.4 \times 10^{10}$ K assuming full disc emission using the distance determined from *Gaia* (Gaia Collaboration 2021).

While the radio peak appears to coincide with an increased optical emission in the *TESS* data, the optical peak was not flagged as a flare event by the automatic flare detection routines. An optical peak at the end of the ASKAP–*TESS* simultaneous observing period was not detected at radio frequencies. Fig. 5 was used to examine whether this notch is a persistent star-spot feature or an individual transient event.

3.2 TIC 55497266 (BPS CS 29520-0077)

TIC 55497266 was also detected in the observation field SB25077. The peak Stokes *I* flux density from a 13 h integrated image was 0.25 ± 0.01 mJy beam^{-1}. Following the same process as carried out for CD-56 1032A, the 10-min imaging revealed variability with a Stokes *I* peak flux density of 2.06 ± 0.14 mJy beam^{-1} (see Fig. 4). There was no associated significant Stokes *V*, *Q*, or *U* emission detected during the observation. A brightness temperature of $1.4 \times 10^{11} \pm 0.1 \times 10^{11}$ K was calculated. Although the simultaneous ASKAP/*TESS* observations covered more than one stellar rotation (see Fig. 4), no flares were seen during this time interval.

3.3 WOH S 2 (TIC 29779873)

WOH S 2 is one of two active M dwarfs detected in the earlier ASKAP observation (SB25035) on 2021-03-20. A Stokes *I* 13 h integrated peak flux density of 0.25 ± 0.03 mJy beam^{-1} was determined where the peak flux density of the 10-min integrated light curve was 1.34 ± 0.07 mJy beam^{-1}. Stokes *V* emission was detected from WOH S 2 (see Figs 3 and 4) with a flux density in the 13 h integrated image of 0.19 ± 0.03 mJy beam^{-1} and a 10-min peak of 0.44 ± 0.09 mJy beam^{-1}. The peak circular polarization fraction of the burst is 32.8 per cent ± 7 per cent. All Stokes *V* emission detected from this source is positive, signifying it is left-hand circularly polarized (LCP). The brightness temperature calculated from these observations is $1.60 \times 10^{12} \pm 0.16 \times 10^{12}$ K. As this value likes above the incoherent emission mechanism, it is plausible that either ECM or gyrosynchrotron could be the emission mechanism. However, gyrosynchrotron cannot be disregarded, as the error on the brightness temperature is high, and the degree of circular polarization is low.

The overlapping *TESS* light curve was captured as *TESS* realigned CCDs on the field after down-linking data, and thus was in coarse pointing mode for the duration of the simultaneous observation. The flux variance is of the order of ±10 per cent. No significant optical flaring activity occurred during this time.

3.4 HD 270712 (TIC 294750180)

This source was detected in both Stokes *I* and *V* during ASKAP observations. HD 270712 is a binary system composing of two active M dwarfs orbiting each other at a separation of ∼50 au (M0 and M1), both of which may be active (Bergfors et al. 2010). The two sources could not be distinguished in either the ASKAP or *TESS* data. A flare was detected in the ASKAP radio light curve, and was visible across the Stokes *V* dynamic spectrum as a short-duration vertical burst (see Fig. 6). The *TESS* light curve for this star was corrupted by instrumental effects and was not analysed further.

There was a weak Stokes *I* detection for this source in the 13 h integrated image. A 100 per cent LCP radio burst was detected. The peak flux density of the 5 min Stokes *V* radio light curve was 1.10 ± 0.01 mJy beam^{-1}. The 13-h Stokes *V* integrated flux was 0.15 ± 0.01 mJy beam^{-1}. The Stokes *I* integrated flux is 0.20 ± 0.02 mJy beam^{-1}. The radio burst visible in the dynamic spectrum in Fig. 6 was not detected in Stokes *I*. As there is no stellar radius calculation for this source no brightness temperature could be calculated. The peak frequency integrated flux of the Stokes *V* burst was measured at 3.2σ significance, while the peak pixel flux within the burst at 800 MHz from the dynamic spectrum was $\sim 2.5\sigma$ (4.66 ± 0.02 mJy beam^{-1}).

3.5 Detection density

We detected 4 M dwarfs in the ASKAP data within a two regions of the sky in 13-h integrated images totalling 60 deg^2. This is a detection rate of 6.67×10^{-2} deg^{-2}. We compare the detection rate of this

[3] https://www.pas.rochester.edu/~emamajek/EEM_dwarf_UBVIJHK_colors_Teff.txt.

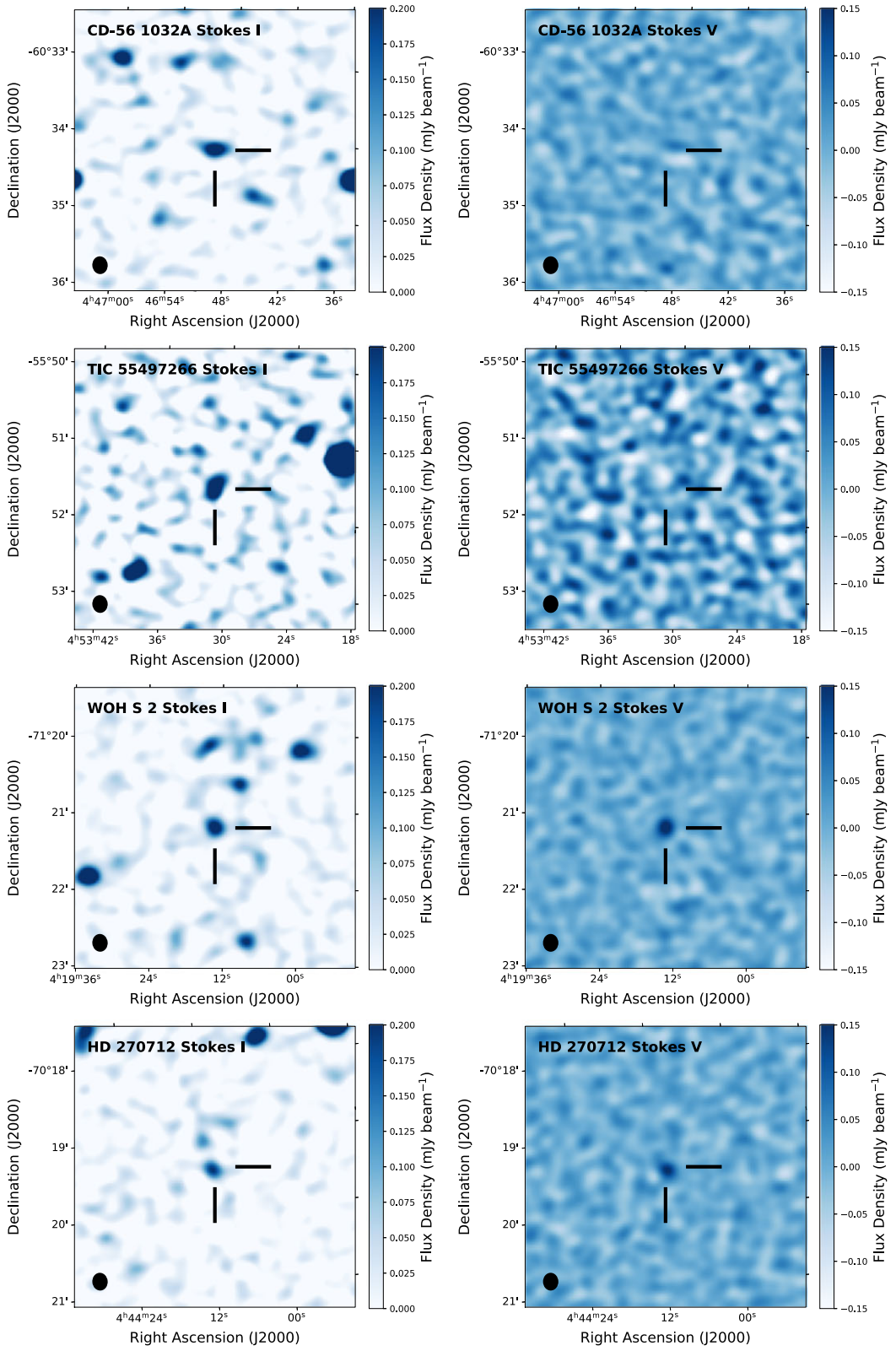

Figure 3. ASKAP 13 h Stokes *I* (left column) and *V* (right column) images of the four detected source coordinates. Source locations are highlighted by cross-hairs, centred on Günther et al. (2020) catalogue coordinates (J2020, proper motion corrected). CD-56 1032A and TIC 55497266 were detected in Stokes *I* only. WOH S 2 and HD 270212 were detected in both Stokes *I* and positive Stokes *V*. The synthesized beam size is illustrated by the black ellipse in the bottom left of each image and is 13.9 arcsec × 11.4 arcsec.

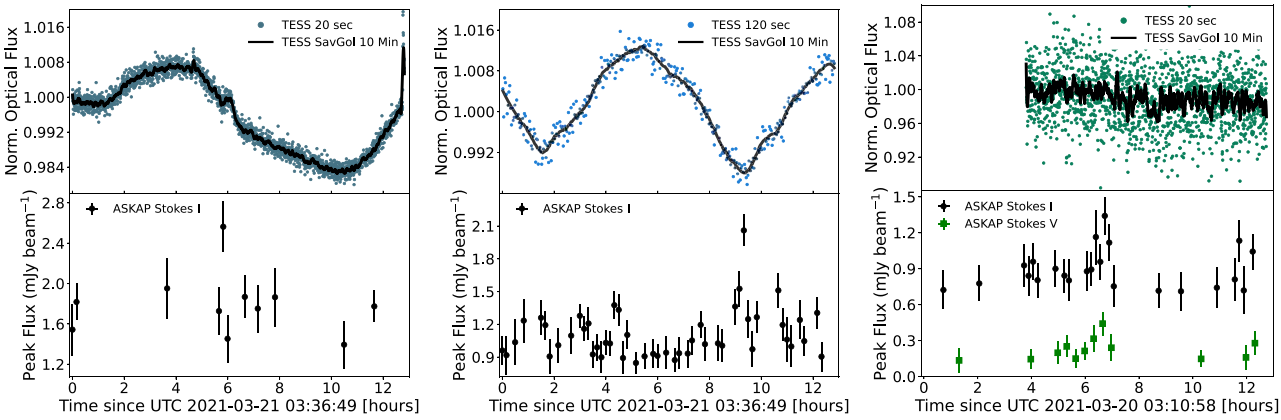

Figure 4. Simultaneous *TESS* (upper panels) and ASKAP (lower panels) Stokes *I* data for CD-56 1032A (left-hand panels); TIC 5549266 (middle panels), and WOH S 2 (right-hand panels). The Stokes *I* data are 4σ above the RMS for all sources, and the Stokes *V* for WOH S 2 is 2σ above the RMS. The *TESS* (upper panel) *y*-axis is the normalized flux for each star.

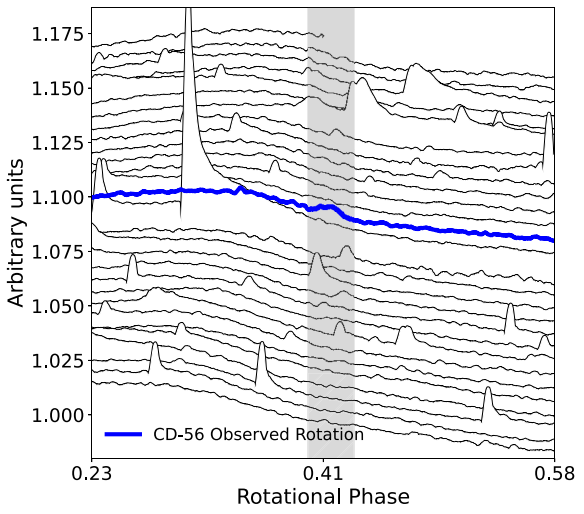

Figure 5. Folded rotation period of CD-56 1032A (0.8531 d) during the full duration of *TESS* Sector 36. The blue line corresponds to part of the time co-observed with ASKAP with the raised notch feature highlighted within the overlapping shaded region. The shaded region corresponds to the start and end time of the raised notch. No other feature occurs within this region at the same point of rotation of the source, which may indicate it is not an evolutionary feature of a star-spot but rather a single active event.

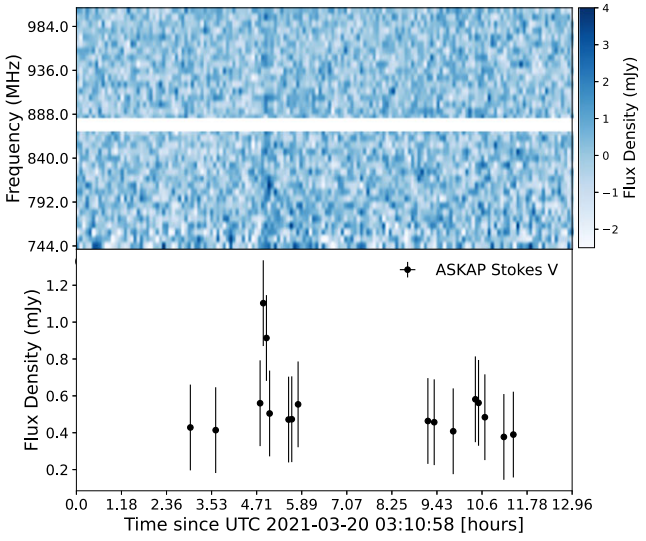

Figure 6. (Top) ASKAP 5-min 8 MHz dynamic spectrum for HD 270712 Stokes *V*. (Bottom) The 2σ Stokes V frequency averaged 5-min time integrated light curve for HD 270712. Note the radio burst at 4.7 h after the beginning of simultaneous ASKAP–*TESS* observations. The integrated flux of the Stokes *V* burst was measured at 3.2σ significance.

work with that reported in Pritchard et al. (2021) for K and M dwarfs of $5.27^{+3.06}_{-2.15} \times 10^{-4}$ deg^{-2} at an RMS of 250 μJy. Scaling this rate assuming a Euclidean source count distribution, the expected surface density at an RMS of 21 μJy is 2.16×10^{-2} deg^{-2}. Comparing this surface density to our rate requires further correction to account for the difference in integration time between our 13-h observations and the 15-min RACS low observations. In addition to the decreased noise threshold and improved sensitivity to faint sources, the longer duration of our observations increases the likelihood of observing short-duration bursts. Furthermore, the regions in the current research were chosen for a high number of high cadence *TESS* active M dwarf targets. We also note that the RACS survey only searched for circularly polarized sources. Two sources in the current research emit with significant Stokes *V* signals, this gives a Stokes *V* surface density for the current research of 3.34×10^{-2} deg^{-2}, closer to that of the value determined in Pritchard et al. (2021) but still significantly higher, likely due to the reasons mentioned above.

We also compare the current research to the detection levels of M dwarfs in Callingham et al. (2021a). Coherent radio emission was detected from 19 M dwarfs in ∼20 per cent of the Northern hemisphere (4125 square degrees). This is a detection density of 4.6×10^{-3} M dwarfs per square degree at 144 MHz. The median sensitivity threshold for these detections was 80 μJy. The higher detection density value in the current work may be attributed to the field selection, or the central observed frequency. Furthermore, gyrosynchrotron is more often observed at frequencies ∼1 GHz, while detections at ∼150 MHz (e.g. LOFAR frequencies) are more likely to be attributed to coherent emission processes such as ECM.

Table 2. Stellar parameters of the four M dwarfs in our sample. Spectral types come from SIMBAD apart from WOH S 2 which is the implied type from the *Gaia* EDR3 ($BP - RP$) colour (Gaia Collaboration 2021) and the relationships of Pecaut & Mamajek (2013). Temperature, radius, luminosity, and mass are taken from the *TESS* Input Catalogue (Stassun et al. 2019) apart from WOH S 2 which come from the *Gaia* colour and mass–radius relationships from Baraffe et al. (2015) and Stassun et al. (2019), Gaia Collaboration (2021) data on low-mass stars. The rotation periods and their error have been derived from all the available *TESS* data presented here.

Star	CD-56 1032 A	TIC 55497266	WOH S 2	HD 270712 A/B
Other name	TIC 220433363	BPS CS 29520-0077	TIC 29779873	TIC 294750180
Classification	M3Ve	M1.5V	M4	M0V/M1Ve
Distance (pc)	11.088 ± 0.002	24.543 ± 0.008	51.88 ± 0.06	21.02 ± 0.02
Effective temp. (K)	3400 ± 160	3600 ± 160	4090 ± 200	3600 ± 160
Radius ($R_\odot$)	0.43 ± 0.01	0.48 ± 0.01	0.24 ± 0.01	–
Luminosity ($L_\odot$)	0.022 ± 0.005	0.034 ± 0.008	0.015 ± 0.003	–
Mass ($M_\odot$)	0.42 ± 0.02	0.48 ± 0.02	0.24 ± 0.02	–
T mag	8.7	10.0	12.5	–
Rotation period (d)	0.854 ± 0.002	0.32442 ± 0.00006	2.623 ± 0.006	0.5254 ± 0.0007
ASKAP Coords. ([RA] deg., [DEC] deg.)	(73.3802, −55.8597)	(71.7072, −60.5692)	(64.8055, −71.3532)	(71.0441, −70.3237)

Table 3. The minimum, maximum, and mean detected radio flux density above 4σ from 10 min integrations for each detected star. The table shows Stokes *I* with Stokes *V* in brackets for WOH S 2 and HD 270712. All values are given in mJy beam^{-1}.

Star	Min. flux	Max. flux	Mean flux $\pm 1\sigma$
CD-56	1.38	2.89	1.72 ± 0.23
TIC 55	0.85	2.06	1.11 ± 0.14
WOH S 2	0.61 (0.24)	1.34 (0.44)	0.81 ± 0.07 (0.30 ± 0.07 LCP)
HD 27	0 (0.37)	0 (1.1)	0 (0.54 ± 0.19 LCP)

4 DISCUSSION

The theoretical limit for brightness temperatures from ECM emission is 10^{12} K (Dulk 1985). When the emission has a brightness temperature higher than this, combined with a high fraction of circular polarization, it can be classified as ECM (Kellermann & Pauliny-Toth 1969; Melrose & Dulk 1982). This classification limit has been used to define the emission mechanism powering radio bursts detected from CR Draconis (Callingham et al. 2021b), UV Ceti (Zic et al. 2019), Proxima Centauri (Zic et al. 2020), and many other M dwarfs (Villadsen & Hallinan 2019; Callingham et al. 2021a). The brightness temperatures calculated for three of the detected stars in this study span an order of magnitude surrounding from 0.56×10^{11} K (CD-56 1032A), 1.4×10^{11} K (TIC 55497266), and 1.6×10^{12} K (WOH S 2). These T_b values lie both below and just above the limit for coherent emission, thus we cannot conclusively state that the detected radio emission from these sources was produced via the ECM process.

While high circular polarization is often considered a distinguishing feature of ECM emission, Hallinan et al. (2008) noted that circularly polarized radio emission may not always be detected where ECM is the dominant production mechanism. Radio emission could be depolarized as it passes through the M dwarf magnetic field, as seen in some solar radio bursts (Melrose 2006). Depolarization also occurs near the solar limb. Reduced polarization of emission can also be caused by a number of factors highlighted by Callingham et al. (2021b), which include coronal scattering and reflections passing through density boundaries.

Brightness temperatures below $\sim 10^{12}$ K may be indicative of gyrosynchrotron emission (Dulk & Marsh 1982). This incoherent process powered by mildly relativistic electrons can be detected at the observed frequencies of 1 GHz. A low degree of circular or linear polarization is often detected from this process. The low degree of circular polarization detected from WOH S 2 is also supportive of gyrosynchrotron as the dominant process (Dulk 1985; Osten & Bastian 2006).

In the case of WOH S 2, a low fraction of circularly polarized radio emission was observed during the radio burst, with a higher brightness temperature ($1.6 \times 10^{12} \pm 6.7 \times 10^{11}$ K) compared to CD-56 1032A and HD 270712. WOH S 2 is a late-type M dwarf with a rotation period 2.5–8 times longer than the other two sources. This may contribute to a lower global magnetic field strength and a reduced ability to depolarize escaping emission. The high brightness temperature and circularly polarized emission detected from WOH S 2 suggest ECM may be the main mechanism. It is possible that a faint optical flare occurred on or near the time of radio emission; however, due to the high noise in the *TESS* light curve, it is not possible to verify this. As the brightness temperature lies on the threshold for ECM, within error constraints, and the polarization fraction is low (<50 per cent), we cannot rule out an incoherent mechanism such as gyrosynchrotron.

Previous research has highlighted that ECM emission may originate from stellar auroral magnetic activity (Kuznetsov et al. 2012; Callingham et al. 2021b). This may be the case with CD-56 1032A and TIC 5549266 as no clear optical counterpart was detected in *TESS* observations. More radio observations at < 1 GHz are required to conclude whether ECM or gyrosynchrotron is the primary mechanism powering radio emission from these stars.

TIC 5549266 exhibits peak radio emission aligning with the full star-spot on-disc. Bright peak emission was not observed on the first rotation; however, so this reduces the likelihood that the star-spot is a stable radio emission source.

The CD-56 1032A *TESS* optical light curve contains a small yet significant increase in brightness during the radio observation. This emission was discounted as a flare event by ALTAIPONY; however, it may be evidence for increased activity on the surface of the star that also produced a radio burst.

The emission from three stars was too faint to produce dynamic spectra, thus there was no detection of signatures suggestive of a drifting radio burst. HD 270712 was detected with a high enough signal-to-noise ratio in Stokes *V* to produce a dynamic spectrum with a faint vertical burst across the full observed frequency band (see Fig. 6).

It is possible that the radio waves originate from regions smaller than the full stellar disc used to calculate these values, leading to increased brightness temperature calculations and further supporting ECM as the driving mechanism behind all detected emission. However, without significant circular polarization detections we

cannot conclude that ECM was observed for CD-56 1032A or TIC 55497266.

Assuming that the brightness temperature calculated is the peak at the time of emission for each source, alternative drivers for CD-56 1032A and TIC 55497266 include plasma and gyrosynchrotron emission. The signature of gyrosynchrotron includes a high brightness temperature with low circular polarization (Dulk & Marsh 1982), while plasma emission is frequently cited as the main driver of radio emission from solar activity (Carley et al. 2021). With no supporting clear optical flare observations, it is difficult to conclude the emission mechanism of any of the stars from this research.

5 SUMMARY

Using simultaneous observations of two regions of the Southern Hemisphere with ASKAP and *TESS*, we detected faint variable radio emission from four M dwarfs. *TESS* light curves of the sources did not highlight any significant optical flare events during the observing period. Radio emission characteristics from CD-56 1023A and TIC 55497266 did not match trends in previous research, with no highly circularly polarized radio bursts indicative of flares or possible stellar CMEs detected. The lack of polarization from these two sources may be due to depolarization occurring in the strong magnetic fields surrounding the stars. The third source, WOH S 2, contained a relatively high degree of circularly polarized emission which supports previous conclusions that a high energy ECM event powered this emission. A faint circularly polarized radio burst was detected from HD 270712. No optical flare was detected with *TESS* for any of the sources. This may suggest that a non-flare event accelerated electrons in the stellar corona, perhaps stellar radio noise storms. It is possible that the low signal detected is continuous quiescent emission from these sources with natural variability.

It is likely that the emission originates from regions smaller than the full stellar disc used to calculate brightness temperature values, which would suggest that ECM is the driving mechanism behind all observed signals. However, without significant circular polarization detections, we cannot conclude that ECM was observed for CD-56 1023A or TIC 55497266. It is also possible that gyrosynchrotron is the mechanism driving the radio emission. Without more information related to the emission (circular or linear polarization, frequency drift), it is difficult to compare our results to previous M dwarf radio detections, or to determine if any emission is linked to stellar flares or CMEs. Further follow-up radio observations with simultaneous high-cadence optical data are required to constrain the physical mechanisms driving radio emission from low-mass stars.

ACKNOWLEDGEMENTS

The Australian Square Kilometre Array Pathfinder is part of the Australia Telescope National Facility which is managed by CSIRO. Operation of ASKAP is funded by the Australian Government with support from the National Collaborative Research Infrastructure Strategy. ASKAP uses the resources of the Pawsey Supercomputing Centre. Establishment of ASKAP, the Murchison Radio-astronomy Observatory, and the Pawsey Supercomputing Centre are initiatives of the Australian Government, with support from the Government of Western Australia and the Science and Industry Endowment Fund. We acknowledge the Wajarri Yamatji as the traditional owners of the Murchison Radio-astronomy Observatory site. Armagh Observatory and Planetarium is core funded by the Northern Ireland Executive through the Dept. for Communities. This paper includes data collected by the *TESS* mission. Funding for the *TESS* mission is provided by the NASA Explorer Program. The *Gaia* archive website is https://archives.esac.esa.int/gaia. JGD would like to thank the Leverhulme Trust for an Emeritus Fellowship. JP was supported by Australian Government Research Training Program Scholarship. JR was supported via the Lindsay Fellowship from AOP and DIAS. DK was supported by NSF grant AST-1816492. We would like to thank the referee for their helpful comments and suggestions.

DATA AVAILABILITY

The ASKAP data (SB25035 and SB25077) used in this paper can be accessed through the CSIRO ASKAP Science Data Archive (CASDA). The *TESS* data for each source in this research are available from the NASA MAST portal.

REFERENCES

Alvarado-Gómez J. D. et al., 2019, ApJ, 884, L13
Alvarado-Gómez J. D. et al., 2020, ApJ, 895, 47
Alvarado-Gómez J. D., Drake J. J., Cohen O., Moschou S. P., Garraffo C., 2018, ApJ, 862, 93
Baraffe I., Homeier D., Allard F., Chabrier G., 2015, A&A, 577, A42
Bergfors C. et al., 2010, A&A, 520, A54
Bochanski J. J., Hawley S. L., Covey K. R., West A. A., Reid I. N., Golimowski D. A., Ivezić Ž., 2010, AJ, 139, 2679
Callingham J. et al., 2021a, Nat. Astron., 5, 1233
Callingham J. et al., 2021b, A&A, 648, A13
Carley E. P. et al., 2021, ApJ, 921, 3
Carley E. P., Hayes L. A., Murray S. A., Morosan D. E., Shelley W., Vilmer N., Gallagher P. T., 2019, Nat. commun., 10, 1
Carley E. P., Vilmer N., Simões P. J., Fearraigh B. Ó., 2017, A&A, 608, A137
Cerruti A. P., Kintner P. M., Jr, Gary D. E., Mannucci A. J., Meyer R. F., Doherty P., Coster A. J., 2008, Space Weather, 6, S10D07
Cornwell T., Voronkov M., Humphreys B., 2012, in Image Reconstruction from Incomplete Data VII, 8500
Crosley M. K. et al., 2016, ApJ, 830, 24
Crosley M. K., Osten R. A., 2018, ApJ, 856, 39
Davenport J. R. A., 2016, ApJ, 829, 23
Dulk G. A., 1985, ARA&A, 23, 169
Dulk G., Marsh K., 1982, ApJ, 259, 350
Fionnagáin D. Ó. et al., 2022, ApJ, 924, 115
Gaia Collaboration, 2018, A&A, 616, A1
Gaia Collaboration, 2021, A&A, 649, A1
Günther M. N. et al., 2020, AJ, 159, 60
Hallinan G., Antonova A., Doyle J. G., Bourke S., Lane C., Golden A., 2008, ApJ, 684, 644
Henry T. J., Jao W.-C., Subasavage J. P., Beaulieu T. D., Ianna P. A., Costa E., Méndez R. A., 2006, AJ, 132, 2360
Hotan A. et al., 2021, Publ. Astron. Soc. Aust., 38, E009
Johnston S. et al., 2008, Exp. Astron., 22, 151
Kellermann K., Pauliny-Toth I., 1969, ApJ, 155, L71
Kochukhov O., 2021, A&AR, 29, 1
Kuznetsov A. A., Doyle J. G., Yu S., Hallinan G., Antonova A., Golden A., 2012, ApJ, 746, 99
Lightkurve Collaboration, 2018, Astrophysics Source Code Library, record ascl:1812.013
Liu H. et al., 2018, Sol. Phys., 293, 1
Lynch C. R., Lenc E., Kaplan D. L., Murphy T., Anderson G. E., 2017, ApJ, 836, L30
Maguire C. A., Carley E. P., McCauley J., Gallagher P. T., 2020, A&A, 633, A56
Marques M., Zarka P., Echer E., Ryabov V., Alves M., Denis L., Coffre A., 2017, A&A, 604, A17
McConnell D. et al., 2020, Publ. Astron. Soc. Aust., 37, E048

McMullin J. P., Waters B., Schiebel D., Young W., Golap K., 2007, in Astronomical Data Analysis Software and Systems XVI, 127
Melrose D., 2006, ApJ, 637, 1113
Melrose D., Dulk G., 1982, ApJ, 259, 844
Metodieva Y. T., Kuznetsov A. A., Antonova A. E., Doyle J. G., Ramsay G., Wu K., 2017, MNRAS, 465, 1995
Morosan D. E., Kilpua E. K., Carley E. P., Monstein C., 2019, A&A, 623, A63
Morosan D., Kumari A., Kilpua E., Hamini A., 2021, A&A, 647, L12
Moschou S.-P., Drake J. J., Cohen O., Alvarado-Gómez J. D., Garraffo C., Fraschetti F., 2019, ApJ, 877, 105
Mullan D., Paudel R., 2019, ApJ, 873, 1
Murphy T. et al., 2013, Publ. Astron. Soc. Aust., 30, E006
Murphy T. et al., 2021, Publ. Astron. Soc. Aust., 38, e054
Nelson G., Melrose D., 1985, Solar Radiophysics: Studies of Emission from the Sun at Metre Wavelengths, 333
Osten R. A. et al., 2010, AJ, 721, 785
Osten R. A., Bastian T., 2006, ApJ, 637, 1016
Osten R. A., Wolk S. J., 2015, ApJ, 809, 79
Pecaut M. J., Mamajeck E., 2013, The Astrophysical Journal Supplement Series, 208.1, 9
Pecaut M. J., Mamajek E. E., 2013, ApJS, 208, 9
Pope B. J., Callingham J. R., Feinstein A. D., Günther M. N., Vedantham H. K., Ansdell M., Shimwell T. W., 2021, ApJ, 919, L10
Pritchard J. et al., 2021, MNRAS, 502, 5438
Raja K. S. et al., 2022, ApJ, 924, 58
Rajpurohit A., Reylé C., Allard F., Homeier D., Schultheis M., Bessell M., Robin A., 2013, A&A, 556, A15
Ramsay G., Kolotkov D., Doyle J. G., Doyle L., 2021, Sol. Phys., 296, 162
Reid H. A. S., Ratcliffe H., 2014, Res. Astron. Astrophys., 14, 773
Ricker G. R. et al., 2015, J. Astron. Telesc. Instrum. Syst., 1, 014003
Schmidt S. J. et al., 2019, ApJ, 876, 115
Schmitt J. H. M. M., Ioannidis P., Robrade J., Czesla S., Schneider P. C., 2019, A&A, 628, A79
Stassun K. G. et al., 2019, AJ, 158, 138
Stepanov A., Kliem B., Zaitsev V., Fürst E., Jessner A., Krüger A., Hildebrandt J., Schmitt J., 2001, A&A, 374, 1072
Vedantham H. et al., 2020, Nat. Astron., 4, 577
Vedantham H., 2021, MNRAS, 500, 3898
Villadsen J., Hallinan G., 2019, ApJ, 871, 214
Wang Y., Tuntsov A., Murphy T., Lenc E., Walker M., Bannister K., Kaplan D. L., Mahony E. K., 2021, MNRAS, 502, 3294
Whiting M., Humphreys B., 2012, Publ. Astron. Soc. Aust., 29, 371
Zic A. et al., 2019, MNRAS, 488, 559
Zic A. et al., 2020, ApJ, 905, 23

This paper has been typeset from a TEX/LATEX file prepared by the author.